

Modulation of Electron Transfer in electrochemiluminescence: Synergistic Utilization of Doping Effects in the Material and Composite Effects of Au in the Core-Shell Structure

Shaopeng Zhang, Mingzhe Jiang, Hongling Li, Wenjin Liang, Wenjing Lai, Haoyi Ren, Chenglin Hong, WeiHua Xu**

School of Chemistry and Chemical Engineering/State Key Laboratory Incubation Base for Green Processing of Chemical Engineering, Shihezi University, China

E-mail: hcl_tea@shzu.edu.cn; 1372730686@qq.com.

1. Reagents and materials

Tetraethoxysilane (TEOS), ammonia ($\text{NH}_3 \cdot \text{H}_2\text{O}$), luminol, formaldehyde solution, manganese chloride tetrahydrate ($\text{MnCl}_2 \cdot 4\text{H}_2\text{O}$), anhydrous ethanol, tetrachloroauric acid ($\text{HAuCl}_4 \cdot 4\text{H}_2\text{O}$), sodium citrate, 2-aminoterephthalic acid ($\text{NH}_2\text{-BDC}$), potassium permanganate (KMnO_4), N,N-Dimethylformamide (DMF), glutaraldehyde, copper chloride dihydrate ($\text{CuCl}_2 \cdot 2\text{H}_2\text{O}$), zinc chloride (ZnCl_2), polydiallyldimethylammonium chloride (PDDA), 1-(3-dimethylaminopropyl)-3-ethylcarbodiimide hydrochloride (EDC), N-hydroxysuccinimide (NHS), 3-aminopropyltriethoxysilanes (APTES), sodium dihydrogen phosphate (NaH_2PO_4), potassium chloride (KCl), and disodium hydrogen phosphate (Na_2HPO_4) were purchased from MACKLIN. Luminol was purchased from Aladdin Reagent Co. Bovine serum albumin (BSA) was supplied by Alfa Aesar. CEA antigen and CEA antibody were supplied by Zhengzhou BioCell Co.Ltd. 5% wt. Nafion was gotten from MACKLIN. Ultrapure water was obtained from milliq system.

2. Apparatus

An ultrasonic cleaner (KQ-250B), an RG-160AT centrifuge (Hunan, China), an X-ray diffractometer (XRD) (D8 Advance, Bruker AG), a DZF-6020 vacuum drying oven (Shanghai, China), and a Zeiss Sigma 300 Scanning Electron Microscope (SEM, Germany) and H-600 Transmission Electron Microscope (TEM, Hitachi, Japan) were used to analyze the morphology of the prepared samples. TEM, Hitachi, Japan) were used to morphologically analyze the prepared samples, Fourier transform infrared spectroscopy (FTIR) analyses were performed on a Perkin-Elmer Spectrum Model GX, X-ray photoelectron spectroscopy (XPS, Thermo ESCALAB 250XI), Ultraviolet-visible (UV-vis) spectrophotometer (UV-3600), and ultraviolet-visible diffuse reflectance test (UV-Vis DRS, PE lambda 750), Electrochemical impedance spectroscopy (EIS) was performed on CHI660E (Shanghai Chenhua).

3. Experimental section

3.1. Synthesis of $\text{SiO}_2\text{:Mn}$

An appropriate amount of $\text{MnCl}_2 \cdot 4\text{H}_2\text{O}$ was dissolved in Solution A, which was a mixture of 9 mL of absolute ethanol and 3 mL of tetraethoxysilane (TEOS), ensuring complete dissolution with the aid of a magnetic stirrer. In another container, a mixed Solution B was prepared by combining 4.5 mL of ammonia water with 21 mL of absolute ethanol, serving as the medium for hydrolysis and condensation reactions. Solution A was slowly and steadily added to Solution B, taking care to avoid vigorous reactions or precipitation. After the addition of Solution A was complete, the mixed solution was stirred for 1 h at room temperature to ensure a uniform reaction. Following the stirring, the mixed solution was allowed to age for 24 h at room temperature to promote the maturation and stabilization of the colloidal particles. After aging, SiO_2 colloids with varying Mn doping ratios were successfully prepared, including SiO_2 , $\text{SiO}_2\text{:0.12\%Mn}$, $\text{SiO}_2\text{:0.6\%Mn}$, and $\text{SiO}_2\text{:1.2\%Mn}$. These colloids were to be used in

subsequent experiments, such as comparing their differences in ECL signal quenching effect.

3.2. Synthesis of Au/SiO₂:0.6%Mn

First, 4 mL of the 24 h aged SiO₂:0.6%Mn colloid was accurately measured and placed in a beaker for later use. Next, a solution containing 0.5 mL of H₂AuCl₄·4H₂O (0.3 mM) was prepared by mixing it with 4 mL of water and 32 mL of ethanol. The prepared H₂AuCl₄ solution was then slowly poured into the beaker containing the aged SiO₂:0.6%Mn colloid, and a magnetic stirrer was used to stir gently for 30 minutes. During the stirring process, 1 mL of 1 M formaldehyde solution was slowly added. Formaldehyde acted as a reducing agent to reduce Au (III) in H₂AuCl₄ to Au (0), forming gold nanoparticles. As formaldehyde was added, the solution color gradually turned yellow, indicating the formation of gold nanoparticles. The mixed solution was then placed at room temperature for aging treatment, which continued for 24 h. The aging process helped to further stabilize and disperse the gold nanoparticles on the surface of the SiO₂:Mn colloid. Immediately following, the mixed solution was washed three times each with ethanol and deionized water to remove any unreacted reagents and possible impurities. After washing, the mixed solution was transferred to a vacuum dryer and vacuum-dried at 60 °C for 5 h to obtain the dried Au/SiO₂:0.6%Mn composite.

3.3. Synthesis of SiO₂:0.6%Mn@MnO₂ with Au/ SiO₂:0.6%Mn @MnO

50 mg of SiO₂:0.6%Mn or Au/SiO₂:0.6%Mn, along with 0.03 g of potassium permanganate, were added to 100 mL of water to ensure they were completely dissolved. Afterward, 1 mL of PDDA was added to the solution. Once the mixture was complete, the solution was transferred into a 180 °C autoclave for a 25 min hydrothermal reaction. After the reaction was finished, the product was washed three times with water and ethanol, respectively, to remove any residual impurities and was then dried. The final step of the experiment involved annealing the dried sample at 180 °C for 5 h.

3.4. Amination of Au/SiO₂:0.6%Mn@MnO

First, the amination of Au/SiO₂:0.6%Mn@MnO was performed. 10 mg of Au/SiO₂:0.6%Mn@MnO powder was uniformly dispersed in 10 mL of absolute ethanol and subjected to ultrasonic treatment for 10 minutes. Subsequently, 10 μL of 3-aminopropyltriethoxysilane (APTES) was added to the solution, and the reaction was stirred under 70 °C water bath for 90 min. After the reaction was complete, the solution was dried for subsequent use.

3.5. Synthesis of NH₂-BDC/luminol

Weighed 0.0354 g of luminol and 0.0724 g of NH₂-BDC and dissolved both in 15 mL of DMF. Subsequently, 1.0 mL of glutaraldehyde (1% wt) was slowly added, and the mixture was stirred for 48 h under light-protected conditions. The NH₂-BDC/luminol solution was prepared and placed in the refrigerator for future use.

3.6. Synthesis of Cu/Zn-MOF/luminol

We added 0.0511 g of $\text{CuCl}_2 \cdot 2\text{H}_2\text{O}$ and 0.04 g of ZnCl_2 to the $\text{NH}_2\text{-BDC/luminol}$ mixed solution from Section 3.5 of the sequence and heated it at $140\text{ }^\circ\text{C}$ for 4 h. After centrifugal washing three times each with water and ethanol, and drying, the desired product was finally obtained.

3.7 Synthesis of Au nanosolutions

1 mL of $\text{HAuCl}_4 \cdot 4\text{H}_2\text{O}$ solution (1% wt) was slowly added to 99 mL of ultrapure water and thoroughly mixed. Subsequently, the mixture was preheated to $100\text{ }^\circ\text{C}$. At this temperature, 2.5 mL of sodium citrate solution (10 mg/mL) was carefully added to the preheated solution. The mixture was continuously stirred and kept at a boil until the solution gradually turned into a wine-red color, indicating the formation of Au nanoparticles. After the color change was completed, heating was stopped, and the solution was allowed to cool naturally to room temperature. Through these steps, the Au nanosolutions was ultimately obtained.

3.8. ECL Testing

The ECL tests were conducted on a CHI660E electrochemical workstation, and the ECL signals were collected using a BPCL ultra-weak luminescence analyzer. A three-electrode system was employed, which included a bare GCE or a modified GCE, a platinum wire, and an Ag/AgCl (saturated KCl) electrode, serving as the working electrode, counter electrode, and reference electrode, respectively. The ECL signals were measured in PBS (pH = 8) containing 6.5 mM H_2O_2 , with the photomultiplier tube (PMT) set at 750 V. The scanning potential ranged from 0 V to 0.8 V vs Ag/AgCl, and the scanning rate was 0.1 V/s.

4. Pictures and tables section

4.1. Elemental analysis of Au/SiO₂:0.6%Mn negative catalyst by EDS

Table S1. Different elemental contents of EDS spectra

Element	E (keV)	Atom (%)
Si	1.739	29.66
O	0.525	69.46
Au	2.120	0.28
Mn	5.894	0.60

4.2. The effect of two oxidation peaks at 1.3 V and 0.9 V (during OER of water) on the ECL intensity of luminol and its electron transfer

To further investigate the effects of these two oxidation peaks on the ECL intensity of luminol and its electron transfer, we performed various data processing on the CV graphs of luminol at different scan rates (Fig. 4) and obtained Fig. 5b and 5c. By analyzing the changes in the magnitude of the linear correlation coefficients, we could

determine whether the impact of the catalyst Cu/Zn-MOF and the reactant H₂O₂ on ECL was surface-controlled (electron transfer) or diffusion-controlled. The greater the correlation coefficient between the luminescent current Ip/V (V is the scan rate), the more the ECL process was surface-controlled (electron transfer), indicating that the diffusion rate was greater than the electron transfer rate; conversely, the greater the correlation coefficient between current Ip/V^{0.5}, the more the ECL process was diffusion-controlled, meaning that the electron transfer rate was greater than the diffusion rate. After carefully comparing the correlation coefficients in **Fig. 5b** and **5c**, we found that the luminescence mechanism of luminol O₂ was mainly diffusion-controlled, while luminol H₂O₂ was more controlled by electron transfer. This implies that the addition of H₂O₂ could promote electron transfer at around 1.3 V (during the ROS generation process), but it had a smaller impact on the electron transfer of luminol. In contrast, adding H₂O₂ as a reactant significantly accelerated the diffusion step, thereby enhancing the ECL signal. In the case of Cu/Zn-MOF as a catalyst carrying luminol, the reaction with H₂O₂ was mainly diffusion-controlled. Comparing the Cu/Zn-MOF/luminol H₂O₂ system with the luminol H₂O₂ system, the results showed that the modified catalyst Cu/Zn-MOF tended to promote electron transfer during the ROS generation process (near 0.9 V in the OER process), thereby initiating electrocatalysis and leading to an enhancement of the ECL signal. This further proved that the 0.9V oxidation peak influenced by the modified catalyst had a more significant effect on the electron transfer of luminol.

4.3. Slope of the Mott-Schottky curve and variation of the flat band potential

Table S2. Slope magnitude of the Mott-Schottky curve and flat band potential

SiO ₂ doped with different Mn contents	Numerical magnitude of the slope of the modified material (/10 ¹¹)	Flat charged level (V _{fb}) (V vs. Hg/Hg ₂ Cl ₂)
SiO ₂	2.085	0.284
SiO ₂ 0.12%Mn	-1.948	2.297
SiO ₂ 0.6%Mn	-0.851	1.377
SiO ₂ 1.2%Mn	2.41	-0.810

The positive or negative slope of the Mott-Schottky (M-S) curve indicates the division between n-type and p-type semiconductors, while the magnitude of the slope corresponds to the concentration of charge carriers. The greater the absolute value of the slope, the higher the concentration of electrons and holes as charge carriers.

Extending the linear region of the material's M-S curve to zero allows for the determination of the flat band potential (V_{fb}). A higher positive value of V_{fb} suggests that the working electrode has absorbed more energy, and consequently, the actual Fermi level (E_{fb}) is lower. This is due to the mismatch of Fermi levels when the semiconductor comes into contact with the solution, causing the energy band to bend. The application of the flat band potential aims to eliminate this band bending phenomenon. Since the Fermi level of the solution phase (usually referred to as the

electrode potential) is relatively stable, the flat band potential can be approximated as the difference between the semiconductor's Fermi level and the solution electrode potential¹. Using the calomel electrode as a reference, the flat band potential can be considered as the Fermi energy level of the semiconductor with respect to the standard calomel electrode. Therefore, an increase in V_{fb} indicates that the working electrode has absorbed more energy, leading to a lower actual E_{fb} .

4.4. Binding energy data for SiO₂:Mn

Table S3. O1s and Si2p binding energy data for SiO₂ with different Mn contents

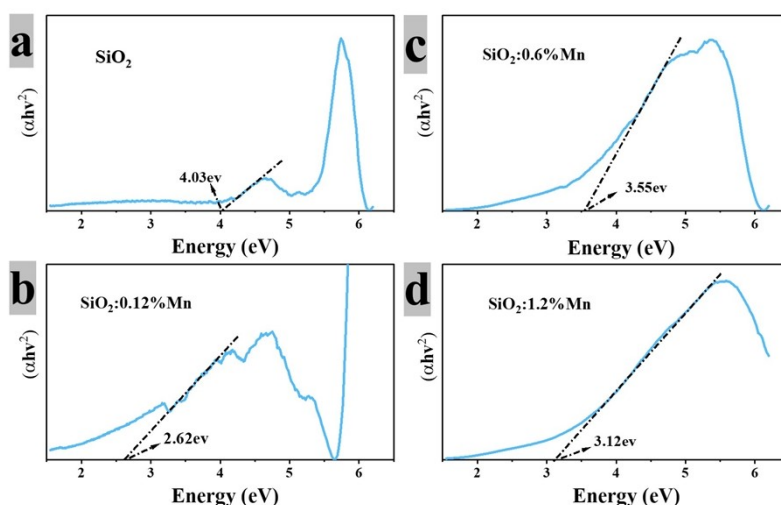
SiO ₂ with different Mn contents	Si 2p (eV)	O 1s (eV)
SiO ₂	103.41	532.67
SiO ₂ :0.12%Mn	103.83	533.18
SiO ₂ :0.6%Mn	103.70	533
SiO ₂ :1.2%Mn	103.25	532.53

According to the data in **Table S3**, we observed that with the increase in Mn content, the Si 2p binding energy of SiO₂ underwent a change. Specifically, SiO₂:0.12% Mn had the highest binding energy, which is attributed to the large number of hole carriers generated in the material due to P-type doping. In P-type doping, Mn acts as a host impurity accepting electrons and forming holes in the material. This shifts part of the electron cloud of Si atoms to maintain electrical neutrality, which in turn reduces the electron cloud density of Si atoms. This redistribution of the electron cloud enhances the attraction of the Si nucleus for the remaining electrons, leading to an increase in the binding energy of the Si atoms.

Conversely, N-type doping produces electron carriers, which can reduce the equilibrium electron cloud density of the internal O atoms in SiO₂, leading to a decrease in the binding energy. As the transition from SiO₂:0.12%Mn to SiO₂:1.2%Mn occurred, the Si 2p binding energy gradually decreased, reflecting the transition from P-type to N-type doping. These results indicate that changes in Mn content affect the type of doping and thus the change in binding energy, which ultimately leads to changes in catalytic activity.

4.5. Tauc plot of SiO₂:Mn obtained from the variation of Fig. 6e

Fig. S1. Tauc plot of SiO₂ doped with different contents of Mn



Tauc plot for SiO₂:Mn shown in **Fig. S1** was derived from the data in **Fig. 6e**. By extrapolating the linear portion of the curve to zero, we were able to determine the bandgap size for the material.

4.6. State density centers determine the catalytic activity of SiO₂:Mn

To further understand the catalytic activity of the material, we can utilize valence band X-ray photoelectron spectroscopy (VB-XPS) testing to determine the position of the valence band center. In VB-XPS testing, the position of the valence band center represents the situation of the density of states (DOS) center, which helps us investigate how different Mn doping contents affect the catalytic activity of SiO₂. As shown in **Fig. 6h**, the valence band center positions for SiO₂, SiO₂:0.12%Mn, SiO₂:0.6%Mn, and SiO₂:1.2%Mn were 5.38 eV, 6.68 eV, 6.78 eV, and 5.22 eV, respectively, with corresponding DOS centers at -5.38 eV, -6.68 eV, -6.78 eV, and -5.22 eV, respectively. The closer the valence band center is to 0 eV (at 0 eV is the energy corresponding to E_{fb}), indicating that the center of density of states rises closer to the Fermi energy level and thus the activity of the material increases. SiO₂:1.2%Mn had the density of states center closest to the Fermi level (0 eV), making it the most active. This is because the high concentration of n-type doping led to an increase in defects and electrons, bringing the density of states center closer to the Fermi level. SiO₂:0.6%Mn had the lowest density of states center (the farthest from 0 eV), corresponding to its lowest activity. Additionally, the density of states centers of SiO₂:0.12%Mn and SiO₂:0.6%Mn were much lower than those of other SiO₂:Mn composites. This is because both SiO₂:0.12%Mn and SiO₂:0.6%Mn are P-type semiconductors, and the generation of holes cause the electron occupation level to move away from the Fermi level, resulting in a significant decrease in the density of states center. In contrast SiO₂:0.12%Mn, the density of states center of SiO₂:0.6%Mn only decreased by 0.1 eV. This can be attributed to the appearance of N-type doping: although the bandgap of SiO₂:0.6%Mn (3.55 eV, see **Fig. S1**) is much larger than that of SiO₂:0.12%Mn (2.62 eV, see **Fig. S1**), theoretically, which results in the density of states center of SiO₂:0.6%Mn being

much lower than that of $\text{SiO}_2:0.12\%\text{Mn}$. However, when transitioning from $\text{SiO}_2:0.12\%\text{Mn}$ to $\text{SiO}_2:0.6\%\text{Mn}$, the electrons produced by N-type doping neutralized some of the hole concentration. This neutralization effect offset the decrease in the density of states center caused by the increase in bandgap, resulting in only a 0.1 eV decrease in the density of states center. Overall, in the $\text{SiO}_2:\text{Mn}$ system, $\text{SiO}_2:0.6\%\text{Mn}$, with the lowest density of states center, exhibited the weakest electrocatalytic activity and was most effective in suppressing electron transfer.

4.7. Comparative experiments of $\text{Au}/\text{SiO}_2:\text{Mn}$ and $\text{SiO}_2:\text{Mn}$

Fig. S2. (a). EIS of Au/SiO_2 and SiO_2 , (b). XPS spectra of $\text{Au}/\text{SiO}_2:0.6\%\text{Mn}$ and $\text{SiO}_2:0.6\%\text{Mn}$

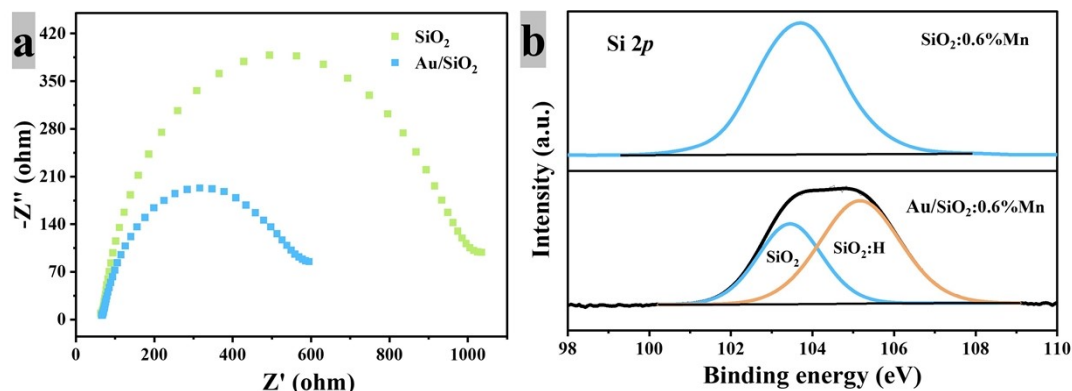
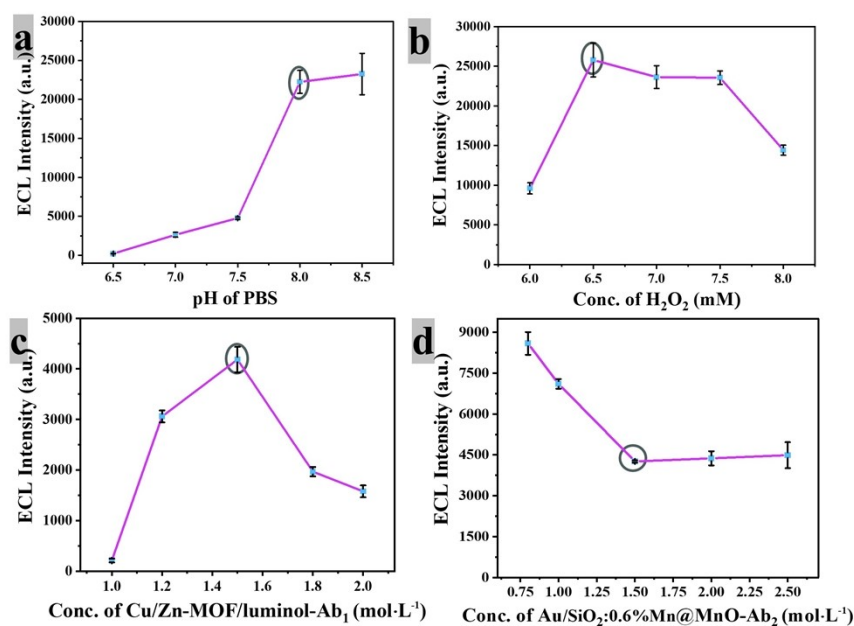


Fig. S2a presents the electrochemical impedance of Au/SiO_2 and SiO_2 . Au/SiO_2 exhibited a smaller electrochemical impedance than SiO_2 , indicating that the electron transfer efficiency of Au/SiO_2 was stronger than that of SiO_2 due to the catalysis of Au. Furthermore in **Fig. S2b**, we similarly observed that $\text{Au}/\text{SiO}_2:0.6\%\text{Mn}$ appeared as a high valence silica-oxygen compound ($\text{SiO}_2:\text{H}$) compared to $\text{SiO}_2:0.6\%\text{Mn}$. This phenomenon further suggests that the electron transfer from SiO_2 to Au occurred, causing changes in the electronic states of silicon and oxygen atoms in SiO_2 , thereby forming $\text{SiO}_2:\text{H}$. This electron transfer may contribute to the catalytic reaction, which is why the complex of Au in a conventional structure can enhance catalytic effects.

4.8. Optimization conditions

Fig. S3. Optimization of experimental conditions (a) PH, (b) concentration of H₂O₂, (c) concentration of Cu/Zn-MOF/luminol-Ab₁, (d) concentration of Au/SiO₂:0.6%Mn@MnO-Ab₂



By utilizing Cu/Zn-MOF to load luminol, we could combine with more primary antibodies to enhance the sensitivity of the sensor. Additionally, to improve the detection performance and stability of the ECL detection technology, we employed Au/SiO₂:0.6%Mn@MnO as the quencher and connected it with the secondary antibody. In the PBS buffer system (as shown in **Fig. S3**), we optimized the pH (**Fig. S3a**), the concentration of H₂O₂ (**Fig. S3b**), the concentration of Cu/Zn-MOF/luminol-Ab₁ (**Fig. S3c**), and the concentration of Au/SiO₂:0.6%Mn@MnO-Ab₂ (**Fig. S3d**). Finally, we obtained the optimal conditions with a pH of 8, a concentration of H₂O₂ of 6.5 mM, and the concentrations of Cu/Zn-MOF/luminol-Ab₁ and Au/SiO₂:0.6%Mn@MnO-Ab₂ were both 1.5 mg/mL.

As shown in **Fig. S3a**, the signal reached its maximum at pH = 8, and there was no significant increase in the ECL signal with further increases in pH. This may be because, at higher pH values, luminol may occupy the active sites on the electrode surface, leading to a change in the ROS generation current from the oxygen evolution reaction (OER) that is not significant. When the concentration of ROS available for reaction on the electrode surface is insufficient, this limits the reaction rate. As shown in **Fig. S3c**, at low concentrations of Cu/Zn-MOF loading, the promotion of luminol luminescence is greater than the effect of the resistance of the MOF material; while in high concentrations of MOF, the luminescence effect is more affected and the stability is decreased due to the high resistance. **Fig. S3d** shows that when using high concentrations of Au/SiO₂:0.6%Mn@MnO as the quencher, the quencher may bind non-specifically with other molecules, forming complexes. These complexes may help stabilize the excited state of luminol, thereby enhancing the luminescence signal, which may lead to an increase in false-positive signals.

4.9. Linear range and detection limits of different methods

Table S4. Comparison of CEA assay with other method

Method	Linear Range	Detection Limit	References
Colorimetry	0.05 - 20 ng/mL	37 pg/mL	2
Capacitors	0.01-10 ng/ml	10 pg/ml	3
Photoluminescence	0.01 - 1 ng/mL	3 pg/mL	4
Photoelectrochemistry	0.01 - 10 ng/mL	1 pg/mL	5
Photothermal	0.015 - 2.4 ng/mL	3.5 pg/mL	6
Electrochemistry	0.005 - 4 ng/mL	1.9 pg/mL	7
Electrochemiluminescence	0.001 - 0.1 ng/mL	0.62 pg/mL	8
Electrochemiluminescence	0.00001 - 5ng/mL	0.539 fg/ml	This work

Reference

1. X. Cui, *Chemistry*, 2017, **80**, 1160-1171.
2. X. Li, X. Lu, L. Zhang, Z. Cai, D. Tang and W. Lai, *Spectrochimica Acta Part A: Molecular and Biomolecular Spectroscopy*, 2024, **315**, 124269.
3. W. Limbut, P. Kanatharana, B. Mattiasson, P. Asawatreratanakul and P. Thavarungkul, *Analytica Chimica Acta*, 2006, **561**, 55-61.
4. X. Yang, Y. Zhuo, S. Zhu, Y. Luo, Y. Feng and Y. Xu, *Biosensors and Bioelectronics*, 2015, **64**, 345-351.
5. B. Zhang, H. Wang, F. Zhao and B. Zeng, *Electrochimica Acta*, 2019, **297**, 372-380.
6. Y. Zhou, S. Lv, X.-y. Wang, L. Kong and S. Bi, *Analytical Chemistry*, 2022, **94**, 14492-14501.
7. A. Shamsazar, M. Soheili-Moghaddam and A. Asadi, *Microchemical Journal*, 2024, **196**, 109643.
8. Y. Huang, J. Lei, Y. Cheng and H. Ju, *Biosensors and Bioelectronics*, 2016, **77**, 733-739.